┌Pure and Applied Geophysics

Spontaneous Rupture Propagation on a Non-planar Fault in 3-D Elastic Medium

HIDEO AOCHI,[1,*] EIICHI FUKUYAMA[2] and MITSUHIRO MATSU'URA[1]

Abstract—We constructed a new calculation scheme of spontaneous rupture propagation on non-planar faults in a 3-D elastic medium using a boundary integral equation method (BIEM) in time domain. We removed all singularities in boundary integral equations (BIEs) following the method proposed by FUKUYAMA and MADARIAGA (1995, 1998) for a planar fault in a 3-D elastic medium, and analytically evaluated all BIEs for a basic box-like discrete source. As an application of the new calculation scheme, we simulated rupture propagation on a bending fault subjected to uniform triaxial compression and examined the effect of fault bend upon the dynamic rupture propagation. From the numerical results, we found that rupture propagation is decelerated or arrested for some combination of inclined angle of the bending fault and absolute value of the fault strength. The most significant effect of bending is the nonuniform distribution of pre-loaded shear stress due to different orientation of the fault plane under a uniform tectonic stress regime. Our results also indicate that low absolute shear stress level is required to progress the rupture propagation ahead of the inclined fault.

Key words: Boundary integral equation, spontaneous rupture propagation, non-planar fault.

Introduction

Large earthquakes generally occur on a complex interacting fault system rather than a simple planar fault, as inferred from the observations of hypocenter distribution of aftershocks and surface fault traces. In order to explain observed strong ground motion and local crustal deformation near the source, one planar fault model cannot often be a good approximation. For example, the 1992 Landers earthquake, California, has been investigated very well from various points of view. AYDIN and DU (1995) observed the surface fault traces of this earthquake and examined the relation between static stress field and local crustal deformation caused by many fault bends. WALD and HEATON (1995) also supplied a fault model

[1] Department of Earth and Planetary Physics, University of Tokyo, 7-3-1 Hongo, Bunkyo-ku, Tokyo 113-0033, Japan. E-mail: matsuura@eps.s.u-tokyo.ac.jp
[2] National Research Institute for Earth Science and Disaster Prevention, 3-1 Tennodai, Tsukuba, Ibaraki 305-0811, Japan. E-mail: fuku@bosai.go.jp
* H. A. is now at Laboratoire de Géologie, École Normale Supérieure, 24 rue Lhomond 75231 Paris Cedex 05, France. E-mail: aochi@geologie.ens.fr

of three planar faults which rotated gradually and intersect with each other, and analyzed the dynamic process of rupture propagation from one fault to another by inverting seismic waveform data. BOUCHON et al. (1998a) estimated a dynamic stress change on the bending fault from the slip history determined by seismic waveform inversion. They reported that stress concentration due to dynamic rupture propagation reached the order of 20 to 30 MPa on the 30-km-long northernmost segment of the fault before rupture started there, and concluded that unfavorable orientation of the fault might have caused the high stress concentration and led to the arrest of rupture.

In the case of the 1995 Kobe earthquake, Japan, rupture seems to start at the discontinuous point of fault segments and propagates bilaterally. YOSHIDA et al. (1996) gave a source model consisting of 2 or several subfaults to explain geodetic and seismic data and SEKIGUCHI et al. (1996) and IRIKURA et al. (1996) also gave a source model of 3 to 5 subfaults for inversion of strong motion data. Based upon the result from seismic inversion analysis, BOUCHON et al. (1998b) have investigated dynamic stress change during the earthquake. Their results show that distribution of shear stress is highly heterogeneous and that its average value is about 3.3 MPa.

The importance of the complex geometrical structure of faults has been long recognized, and several seismologists have tried modeling spontaneous dynamic rupture propagations on non-planar faults. Using finite difference methods (FDM), for example, HARRIS and DAY (1993) and KASE and KUGE (1998) simulated parallel or perpendicular strike-slip faults in 2-D medium, and subsequently HARRIS and DAY (1999) and MAGISTRALE and DAY (1999) investigated them in 3-D medium. However these approaches are limited in fault geometry due to the spatial grid. On the other hand, the boundary integral equation method (BIEM) enables us to handle complicated fault geometries such as bending and branching. However, since this kind of computation requires complex and advanced techniques with high performances to estimate stress field accurately, as well as to treat numerous freedoms, modeling of dynamic rupture process on complex non-planar faults in 3-D medium is not well established. KOLLER et al. (1992), TADA and YAMASHITA (1996, 1997), KAME and YAMASHITA (1997), BOUCHON and STREIFF (1997) and SEELIG and GROSS (1997) have simulated spontaneous dynamic rupture propagation on preexisting non-planar faults with different boundary integral equations (BIEs) in a 2-D framework. KAME and YAMASHITA (1999a,b) and SEELIG and GROSS (1999a,b) have applied their methods to the problem that rupture proceeds along unknown paths in 2-D. Further, TADA et al. (2000) have formulated a BIE for arbitrary 3-D non-planar faults, removing any singularities in time domain.

One of our aims in this paper is to construct a numerical simulation scheme of spontaneous dynamic rupture propagation for non-planar faults in 3-D elastic medium. The mathematical method developed here is based on a stress BIEM in time domain which rises from COCHARD and MADARIAGA (1994) and FUKUYAMA and MADARIAGA (1995). Since they have formulated BIEs directly for stress

components instead of displacement field removing any strong singularities, their methods enable one to estimate stress field accurately on the fault to simulate spontaneous rupture propagation successfully. First, we extend the on-plane BIEs for a 3-D planar fault, derived by FUKUYAMA and MADARIAGA (1995, 1998), to estimate stress field at an arbitrary point in 3-D medium. Next, we discretize the BIEs and analytically evaluate them for a box-like source element. Finally, using the numerical computation scheme constructed here, we simulate spontaneous rupture propagation on a bending fault in 3-D medium, and discuss the dynamic effects of the geometry such as a fault bend.

Mathematical Formulation Based on 3-D BIEM

Regularization of Boundary Integral Equation

In this section, we give a theoretical framework of numerical computation using BIEM. In order to describe a non-planar fault in 3-D medium, we may take two methodologies. The first one, which is shown in Figure 1(a), is to describe the fault shape exactly by introducing a curved local coordinate system (TADA et al., 2000). This, however, will lead to a very complicated formulation in discretized form, which looks very difficult to compute numerically. Another way that we use here is to approximate a curved fault surface with a combination of small planar patches as shown in Figure 1(b). In this case, the stress on a planar patch (thick line) can be attributed to the slip on the same patch (thick line) through the on-plane kernel, which is already derived by FUKUYAMA and MADARIAGA (1995, 1998), and to those on the other patches (thin lines) through off-plane kernels. TADA and YAMASHITA (1996) pointed out that in the case of a 2-D in-plane shear fault, a smoothly curved crack (Fig. 1(a)) and its approximate expression with a series of small line patches (Fig. 1(b)) produce different normal traction distributions on the
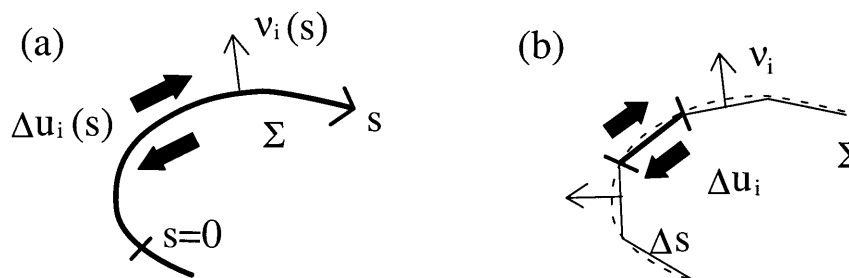

Figure 1
Two representations of a curved fault Σ. (a) Description of a fault by introducing curved local axis (s) along the fault. (b) Approximation of a curved fault with a series of small planar fault elements (Δs). In this case, off-plane stress expression for a flat source is required with the geometry in Figure 2.

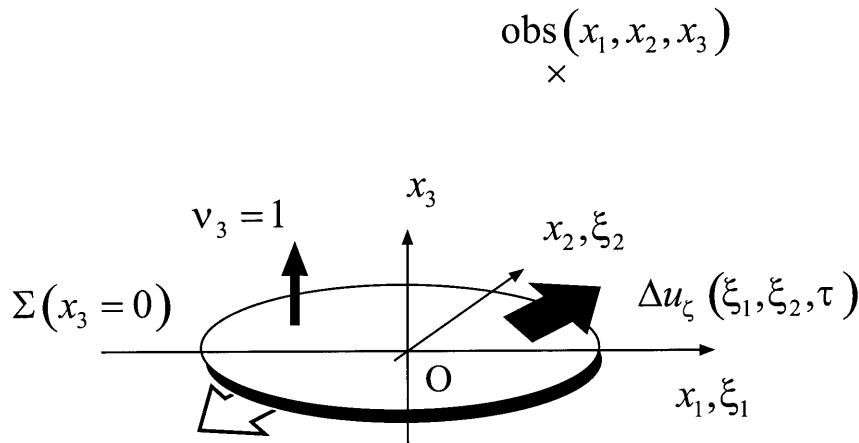$$\text{obs}\left(x_1, x_2, x_3\right)$$
$$\times$$

Figure 2

Geometry of the coordinate system with a fault plane $x_3 = 0$ and its slip discontinuity $\Delta u_\zeta(\vec{\xi}, \tau)$.

fault. Thus we should treat the paradox very carefully in 3-D BIEM, too. In this study, we use a simple slip-weakening law as a fracture criterion, which has no explicit dependence on normal traction.

Now, we derive the expressions of off-plane stress components for a planar fault and then obtain the analytical discrete off-plane kernel suitable for numerical simulation. It usually begins with a representation theorem such as equation (3.2) in AKI and RICHARDS (1980). The displacement field $u_i(\vec{x}, t)$ in a (x_1, x_2, x_3)-coordinate system is written by a spatio-temporal convolution of slip discontinuity $\Delta u_j(\vec{\xi}, \tau)$ over the fault Σ

$$u_i(\vec{x}, t) = \int_{-\infty}^{t} d\tau \int_{\Sigma} \Delta u_j(\vec{\xi}, \tau) c_{jkpq} v_k(\vec{\xi}) \frac{\partial G_{ip}(\vec{x} - \vec{\xi}, t - \tau)}{\partial \xi_q} \, d\Sigma \tag{1}$$

where $\vec{x}$ and t denote position and time at a point in the medium, and $\vec{\xi}$ and τ are position and time at a point on the fault Σ. $G_{ip}(\vec{r}, t - \tau)$ is a Green's function, v_k is normal vector of Σ, and c_{ijkl} are elastic coefficients. We define hereafter that Latin and Greek subscripts vary from 1 to 3 and 1 to 2, respectively, $r = \|\vec{r}\| \equiv \|\vec{x} - \vec{\xi}\|$, $\gamma_i \equiv (x_i - \xi_i)/r$, a comma between subscripts denotes spatial derivatives $\partial/\partial \xi_i$, and an overdot indicates time derivative $\partial/\partial \tau$. We also use the summation convention rule.

We assume that a planar fault is embedded on the $x_3 = 0$ plane in a 3-D homogeneous, isotropic and infinite elastic medium as shown in Figure 2. Slip discontinuity occurs only on the fault without tensile element ($\Delta u_3 \equiv 0$) after $t = 0$. As long as we consider shear rupture on the fault-like earthquakes, the mathematical formulation under these assumptions is enough to model any fault with arbitrary structure and shape in 3-D. The Green's function in equation (1) is called

"Stokes tensor," the concrete expression of which is given by equation (A-1) in Appendix A. For the stress representation obtained by spatial derivatives of equation (1)

$$\tau_{pq}(\vec{x}, t) = -\int_0^t \int_\Sigma \Delta u_\zeta(\vec{\xi}, \tau) c_{\zeta 3 st} c_{pqin} \frac{\partial^2}{\partial x_n \partial x_t} G_{is}(\vec{r}, t - \tau) \, d\Sigma \, d\tau, \qquad (2)$$

we use a regularization method similar to that used by COCHARD and MADARIAGA (1994) and FUKUYAMA and MADARIAGA (1995, 1998) for removing very strong singularities due to the second derivatives of Green's function in equation (2). Applying the techniques of Laplace transforms in time and the integration by parts, we obtain the regularized expression of stress in the form of convolutions of some derivatives of slip with weak singularities. In Appendix A, we briefly explain the derivation for the 3η element and list the final expressions for other components. All the expressions derived here are consistent with the special case of the general formulation for arbitrary shaped fault in 3-D medium derived by TADA *et al.* (2000), although they were independently formulated. Our equations are suitable for further numerical computations.

Discretization

For numerical simulations we discretize the slip velocity field on the fault with the box-like constant functions. We assume constant slip velocity within a spatio-temporal grid (spatial grid size $= \Delta s \times \Delta s$ and temporal interval $= \Delta t$)

$$\Delta \dot{u}_\zeta(\vec{\xi}, \tau) = \sum_{l,m,n} V_\zeta^{mn} d(\xi_1, \xi_2, \tau; \xi_1^l, \xi_2^m, \tau^n), \qquad (3)$$

where function $d(\cdot)$ consists of 8 Heaviside functions $H(\cdot)$

$$d(\xi_1, \xi_2, \tau; \xi_1^l, \xi_2^m, \tau^n) = \begin{cases} 1 & \text{for } \xi_1^l - \Delta s/2 \le \xi_1 < \xi_1^l + \Delta s/2 \\ & \text{and } \xi_2^m - \Delta s/2 \le \xi_2 < \xi_2^m + \Delta s/2 \\ & \text{and } \tau^n - e_t \Delta t \le \tau < \tau^n + (1 - e_t)\Delta t \\ 0 & \text{otherwise} \end{cases} \qquad (4)$$

where e_t $(0 \le e_t \le 1)$ is the time collocation coefficient appeared in COCHARD and MADARIAGA (1994) and discussed in detail by TADA and MADARIAGA (2000). Therefore we have to obtain discrete kernels of regularized BIEs, equations (A-4), (A-5), (A-6) and (A-7), for a basic Heaviside function in slip velocity field;

$$\Delta \dot{u}_\zeta(\vec{\xi}, \tau) = V_\zeta H(\xi_1, \xi_2, \tau). \qquad (5)$$

We analytically evaluate all the integrals, and the details of expressions are summarized in Appendix B.

Finally, we can write the discrete boundary integral equations in the following form

$$\tau_{pq}(\check{x}, t) = \frac{\mu}{4\pi\beta} \sum_{\zeta=1}^{2} \sum_{l,m,n} P_{pq/\zeta}(\vec{r}, t - \tau^n) V_\zeta^{lmn} \tag{6}$$

where (l, m, n) represents the discrete position (l, m) in (ξ_1, ξ_2)-coordinate and time n of a source grid, and $P_{pq/\zeta}$ is a discrete kernel depending on the position vector $(\vec{r} = (x_1 - \xi_1^l, x_2 - \xi_2^m, x_3)^T)$, the time lag $(t - \tau^n)$, the slip velocity direction (ζ), and the stress component (pq). Stress components on the left-hand side of equation (6) are usually estimated at the center of the spatial grid on the fault, and can be freely estimated for time t as we will discuss below.

Discretization Parameters

As for this discretization method in equation (4), it is well known that there exist two parameters for discretization: the Courant-Friedrichs-Lewy (CFL) ratio w_c and the time collocation coefficient e_t. The CFL ratio w_c is defined by $w_c \equiv c\Delta t/\Delta x$, where c is the velocity of *P*-wave (α) or *S*-wave (β). It controls the length of time step Δt relative to a given spatial grid size Δs. The time collocation coefficient e_t defines the relative location of the time $(t = t^k)$ within a time step Δt. For example, the time to evaluate stress corresponds to the beginning of the current time step $(t^k, t^k + \Delta t)$ for $e_t = 0$, and is collocated at the end between $(t^k - \Delta t, t^k)$ for $e_t = 1$. COCHARD and MADARIAGA (1994) used $w_\beta = 0.5$ and $e_t = 1$ for 2-D anti-plane problems, and KAME and YAMASHITA (1997) used $w_\alpha = 0.5$ and $e_t = 1$ for 2-D in-plane problems. In those situations, the current slip velocity on a grid (V_ζ^{ijk}) effects the stress value on its own grid within its own time step (τ_{pq}^{ijk}), by expressing the point and time $(\check{x}; t)$ as a discrete form $(x_1^i, x_2^j, x_3; t^k)$ in the similar expression for the discretized source $(\xi_1^l, \xi_2^m, 0; \tau^n)$. Thus we can extract the instantaneous term explicitly out of equation (6) as

$$\tau_{pq}^{ijk} = \frac{\mu}{4\pi\beta} \sum_{\zeta=1}^{2} \left[P_{pq/\zeta}^{000} V_\zeta^{ijk} + \sum_{l,m,n} P_{pq/\zeta}^{(i-l)(j-m)(k-n)} V_\zeta^{lmn} \right], \tag{7}$$

where the instantaneous kernel $P_{pq/\zeta}^{000}$ exists only in the 3ζ component for shear source V_ζ, and $P_{pq/\zeta}^{(i-l)(j-m)(k-n)}$ is the discrete kernel of $P_{pq}/\zeta(\vec{r}, t - \tau^n)$. Consequently we can solve the above equation on each spatial grid independently, i.e., using an explicit scheme. FUKUYAMA and MADARIAGA (1998) also examined the stability of numerical computations depending upon the CFL ratio, and reported that the value of w_α should be less than 0.5 for the numerical computations of 3-D planar faults using the explicit schemes. TADA and MADARIAGA (2000) investigated the stability of numerical computations which depend on both the CFL ratio w_α and

the time collocation coefficient e_t for all modes in 2-D problems, and reported that the best combination of the two parameters is localized. With the explicit discrete BIE (7), we will evaluate the stress at the end of one time step, assuming $e_t = 1$ and $w_\alpha = 0.5$.

Fault Constitutive Relation and Normalization

Since the stress is a function of the current slip velocity in the explicit BIE (7), we can mathematically give various types of the fault constitutive relation, e.g., slip-dependent friction law or velocity-dependent friction law, as a fracture criterion on the fault. In this paper we introduce a slip-weakening law defined by

$$\sigma(w) = \tau_r + \Delta\tau_b(1 - w/D_c)H(D_c - w), \qquad (8)$$

where σ is shear strength, w is net slip on the fault, τ_r is residual stress level, and $\Delta\tau_b$ and D_c are the constitutive parameters called the breakdown strength drop and the critical weakening displacement, respectively. When shear rupture occurs on the fault, some fraction of the total stress stored there is released with the progress of fault obeying equation (8). This type of the constitutive relation during shear fracture was originally proposed by IDA (1972) and PALMER and RICE (1973), observed in laboratory experiments by OKUBO and DIETERICH (1984) and OHNAKA et al. (1987), theoretically modeled by MATSU'URA et al. (1992) and also inferred in the field by IDE and TAKEO (1997) and Bouchon et al. (1998b) through seismological data analysis.

Based on the slip-weakening law, we normalize the equations by the critical slip displacement D_c, the breakdown strength drop $\Delta\tau_b$, and initial crack size L, and then introduce a normalization constant Υ

$$\Upsilon = \frac{\alpha}{4\pi\beta}\frac{\mu}{\Delta\tau_b}\frac{D_c}{L}. \qquad (9)$$

Furthermore we normalize time with travel time of P wave over an initial crack, $T_\alpha = L/\alpha$, and then slip velocity V_ζ is normalized with $V_\alpha = D_c/T_\alpha$. For example, taking $D_c = 10$ cm, $\Delta\tau_b = 10$ MPa, $L = 400$ m and shear modulus $\mu = 20$ GPa, then $\Upsilon \approx 0.07$ which has almost the same value as that proposed by MATSU'URA et al. (1992), ELLSWORTH and BEROZA (1995), and OHNAKA (1996). When we approximate the initial grid size L with 5 grids, Δs becomes 80 m and Δt is 0.01 s ($T_\alpha = 0.1$ s) for an assumed P-wave velocity $\alpha = 4$ km/s. As a result, the normalized slip velocity $V_\alpha = 1$ m/s.

Explicit Time Stepping Scheme

We explain the method of numerical computation based on the BIE in equations (7) and (8). For simplicity, we restrict the direction of slip vector to one

direction on the fault. If slip occurs in the ξ_1 direction, we have only to consider $\Delta u_1'$ and τ_{31}'. Here we use a prime (') to denote the quantities in the local coordinate (ξ_1, ξ_2, ξ_3) fixed on the non-planar fault ($\xi_3 \equiv 0$).

Hereafter we use the normalized form of BIE and apply the same symbol V_ζ to denote the normalized slip velocity instead of equation (7). At a time step k, we have known all past slip velocities $V_1'^{lmn}$ ($n \leq k - 1$). On some fault patch (i, j) in the local coordinate (ξ_1, ξ_2), the BIE and the general fracture criterion are written in the normalized form

$$T_{31}'^{ijk} = T_{31}^{0}{}' + \Upsilon \left[P_{31/1}^{000} V_1'^{ijk} + \sum_{n=0}^{k-1} \sum_{l,m} P_{31/1}'^{ijk:lmn} V_1'^{lmn} \right] \qquad (10)$$

$$S^{ij} = T_r + (1 - W_1'^{ijk})H(1 - W_1'^{ijk}). \qquad (11)$$

Here we express all the normalized stresses, strength and slip as T, S and W instead of τ, σ and w, respectively, and $T_{31}^{0'}$ is a pre-loaded initial shear stress on the fault. Note that $P_{31/1}'^{ijk:lmn}$ is no longer the same as $P_{31/1}^{(i-l)(j-m)(k-n)}$ in equation (7) since we consider it on the non-planar faults. For the above equations, in general, there are two different states which depend on current slip velocity $V_1'^{ijk}$. When the fault is stuck ($V_1'^{ijk} \equiv 0$), shear strength is required to be larger than applied shear stress ($S_{ij} > T_{31}'^{ijk}$). On the other hand, during fracturing ($V_1'^{ijk} \neq 0$), shear strength and applied shear stress must be equal ($S^{ij} = T_{31}'^{ijk}$). Since the unknown parameter is only the current slip velocity $V_1'^{ijk}$ at the time k, we can solve the equation one by one for every fault patch (i, j). Then we continue this procedure at the next time step $(k + 1)$.

Later we provide 61×61 grids on the fault and continue calculating until the rupture front reaches the end of the computation region. We used Origin 2000 (R 10000, 250 MHz) at Earthquake Information Center of Earthquake Research Institute, University of Tokyo, Japan, and it takes more than 4 hours CPU time to calculate 120 time steps directly. It takes a much longer time than that for a 3-D planar fault, because of the anti-symmetry of the kernels. We have to calculate the kernels between each two points on the non-planar fault, so that more memory is required at the same time. We are able to shorten the computation time to about 30 minutes for the same problem shown in later sections by using FFT technique for convolution, regarding one spatial axis along which the fault structure is univariable (i.e., ξ_2-direction), though it requires about 2 GB memory which is generally twice as many as that without the FFT technique.

Model Setting

Fault Geometry and Initial Stress Field

We consider a simple physical situation in which a bending fault is embedded in the uniform triaxial compression field produced by principal deviatoric stress $\Delta\sigma_1$,

$\Delta\sigma_2$ and $\Delta\sigma_3$ with $\Delta\sigma_1 > \Delta\sigma_2 > \Delta\sigma_3$. Here we take compression to be positive. The fault consists of a primary planar part on the $x_1 x_2$ plane, where the applied shear stress has a maximum value, and a secondary bending part off the $x_1 x_2$ plane. Both the direction in which the fault bends and the maximum shear stress loads are taken to be parallel to the x_1 axis, and the fault shape is invariant toward the x_2-axis.

Now we introduce a local coordinate system (ξ_1, ξ_2, ξ_3) fixed on the bending fault, taking the ξ_1 axis along the direction of bending, the ξ_3 axis normal to the local fault, and the ξ_2 axis perpendicular to them, namely, parallel to the x_2 axis. For simplicity, the direction of fault slip is presumed to be parallel to the local ξ_1 axis, that is, the bending direction of the fault. Then the shear stress driving the fault slip is the τ'_{31} component defined in the local coordinate system. In the present situation (uniform triaxial compression), the applied $\tau_{31}^{0\prime}$ component on the fault can be written as

$$\tau_{31}^{0\prime} = \frac{1}{2}(\Delta\sigma_1 - \Delta\sigma_3)\cos 2\theta \qquad (12)$$

where θ is the angle of inclined fault measured from the primary planar fault ($x_1 x_2$ plane) counter-clockwise. Equation(12) gives the initial stress condition for numerical simulation of dynamic rupture propagation.

We introduce a parameter S that relates the slip-weakening features and applied shear stress. S is defined by $(\tau_p - \tau_{31}^{0\prime})/(\tau_{31}^{0\prime} - \tau_r)$ following DAS and AKI (1977) and DAY (1982), where the peak strength is defined by $\tau_p \equiv \tau_r + \Delta\tau_b$. This parameter can vary on the fault and controls the velocity of rupture propagation. In this paper we take $S = 1/3$ on the primary plane ($\theta = 0$). This value of S is slightly larger than the critical value for which rupture propagation is initiated under the circumstances we gave.

For each simulation, we assume that the values of τ_r and τ_p are constant over the fault except for the region of a given initial crack. Then only the applied shear stress $\tau_{31}^{0\prime}$ varies along the curved ξ_1 axis following equation (12). We indicate the relation between the absolute stress level τ_r and the applied shear stress $\tau_{31}^{0\prime}$ in Figure 3 for three different cases of residual stress, (a) $\tau_r = 5\Delta\tau_b$, (b) $2\Delta\tau_b$ and (c) 0. $\tau_{31}^{0\prime}$ decreases as the inclined angle θ through equation (12). In the case of $\tau_r = 2\Delta\tau_b$, the applied shear stress (thick curved line) given by equation (12) crosses the residual stress level (dotted straight line). On the primary plane ($\theta = 0$) including an initial crack, the initial stress is certainly loaded at a level between τ_r and τ_p, that is, $0 \le S \le 1$. However, as the angle of inclined fault θ increases, the applied shear stress decreases below the residual stress level. In such a region, the shear stress would not be released but be stored, if rupture occurred. In the case of $\tau_r = 0$, which corresponds to the case of tensile rupture or sliding without friction, the applied shear stress is
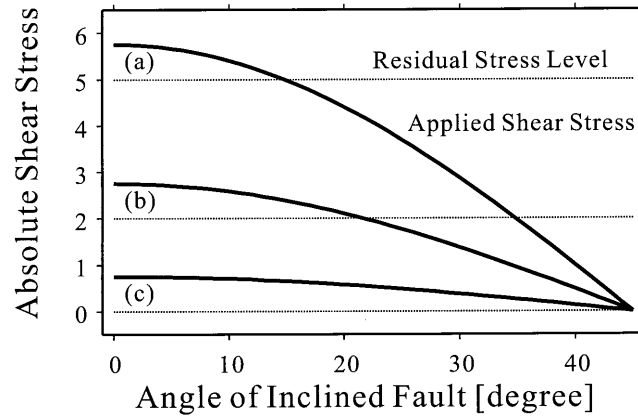
Figure 3
Relation between the absolute residual stress level τ_r and the applied shear stress $\tau_{31}^{0}{}'$ as a function of the angle of the inclined fault θ. The vertical axis is normalized by the breakdown strength drop $\Delta\tau_b$. Thick lines are applied shear stress τ_{31}^{θ} from equation (12) and dotted lines are assumed residual stresses (a) $\tau_r = 5\Delta\tau_b$, (b) $2\Delta\tau_b$ and (c) 0, respectively. In all cases, we take $S = 1/3$ on the plane of $\theta = 0°$.

always above the residual stress level unless $|\theta| \geq \pi/4$, and therefore a positive stress drop occurs to accelerate rupture propagation. When the residual stress level increases, the positive stress drop region becomes narrow, consequently it is expected to become more difficult for the rupture to propagate beyond the fault bend. This suggests that the absolute stress level would be a strong constraint for dynamic rupture propagation on a bending fault.

Furthermore, we should consider the effect of dynamic stress change due to the propagation of elastic waves, which is one of the most important purposes of this study. Perturbation of stress is carried by the P wave first and by the following S wave, and stress remains at static level after the dynamic disturbance finishes. This effect will be examined in detail through numerical simulations in the following section.

In Figure 4, we show an example of a bending fault model in which the left panel represents the applied shear stress field $\tau_{31}^{0}{}'$ and the right panel is the strength distribution τ_p at the beginning of the simulation ($t = 0$). Both are normalized by the breakdown strength drop $\Delta\tau_b$. Annotations on the spatial axes are normalized by grid size Δs, and their origin are located at the center of the initial crack. The initial crack diameter is taken to be 5 grids, that is, $L = 5\Delta s$. Inside the initial crack, the peak strength is lower than the applied initial stress and the breakdown strength drop is half of that outside. The fault bend starts at the 11th grid along the ξ_1 axis and is approximated with an arc whose radius is about $20\Delta s$, though we also approximate it with a series of small planar patches, that is, 10 grids for $\theta = \pi/6$, for example. We also consider a kinked fault which abruptly bends at 11th grid
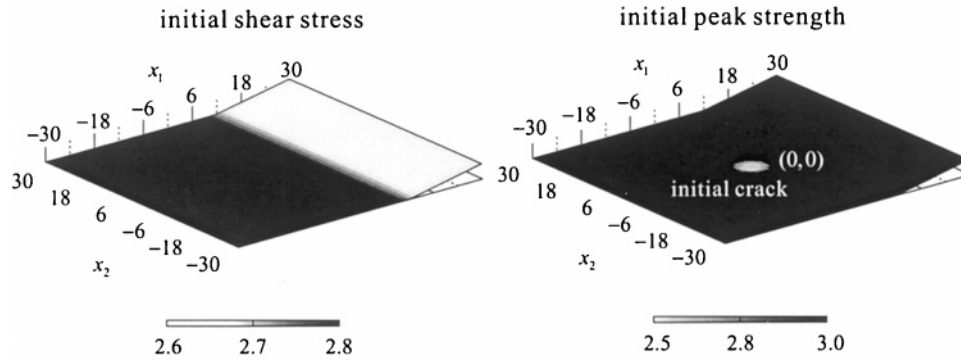
Figure 4
An example of a bending fault. The fault bends around $x_1 = 10.5$ and the bending direction finally changes ($\theta = \pi/18$) from the primary plane. Coordinate is normalized by grid size Δs. The left figure is applied shear stress $\tau_{31}^{0\prime}$ and the right one is assumed peak strength distribution σ for residual stress level $\tau_r = 2\Delta\tau_b$. We assume a circular crack, weak zone, at the center, to initiate rupture propagation. This is the initial condition of the simulation shown in Figure 5(a).

instead of the curved fault. Its final direction of the inclined fault (θ) is changed from $\pi/18$ to $\pi/2$.

Results of Numerical Simulation

Snapshots of Rupture Propagation

A series of snapshots in Figure 5 shows the evolution of slip velocity V_1' (the first row of each group) and shear stress τ_{31}' (the second row) for two bending fault models with different final angles of the inclined secondary fault (a) $\theta = \pi/18$, corresponding to the model as shown in Figures 4, and (b) $\theta = \pi/6$, respectively. The numbers along both axes represent the grid number on the $\xi_1\xi_2$ plane and fault starts bending at $\xi_1 = 10.5$. Ruptures propagate symmetrically on the primary planar fault until the rupture front reaches the bending portion. In the case of a small angle of bending ($\theta = \pi/18$), the rupture continues expanding beyond the bending portion, although expansion of the rupture area in the ξ_2 direction is decelerated by the bend, compared to that on the primary planar fault. When the angle of bending is large, on the other hand, the rupture is nearly arrested at the bending portion. At time step $t \sim 100$, the rupture front reaches the left edge of the computation region. However, its disturbance does not arrive at the opposite side of the crack tip during the calculation.

Figure 6 shows the slip velocities as a function of time step at 3 points, $(\xi_1, \xi_2) = (5, 5)$, $(15, 0)$ and $(12, 12)$, on the fault models of (a) $\theta = \pi/18$ and (b) $\pi/6$, corresponding to Figures 5(a) and (b), respectively. $(\xi_1, \xi_2) = (5, 5)$ is on the
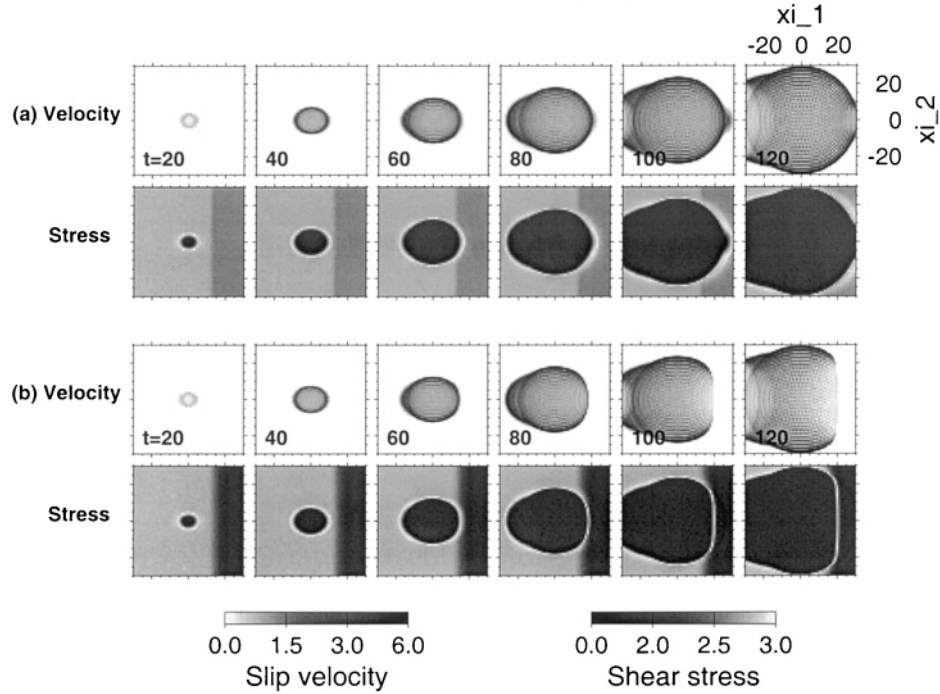
Snapshots of rupture propagation

Figure 5
Two computations with different angles of the inclined fault (a) $\theta = \pi/18$ and (b) $\pi/6$. Upper and lower columns of each panel show slip velocity and shear stress, respectively.

primary fault plane near the initial crack, $(15, 0)$ and $(12, 12)$ are on the curved portion. We observe that the slip velocities are disturbed for each points. However, the magnitude of the disturbance is relatively small compared to the maximum slip velocity which appears just after the passages of the rupture front. That is why the disturbance may not affect the rupture propagation. When the disturbance becomes too large to further continue calculation with BIEM, we should re-scale the slip-weakening distance (D_c) in order to make D_c large enough comparing to spatial grid interval (FUKUYAMA and MADARIAGA, 2000; LAPUSTA *et al.*, 2000). Moreover a numerical experiment using a twice-higher resolution for both space and time leads to the same results as those presented here. This indicates that the numerical solution converges adequately and the numerical oscillations do no affect the ultimate results.
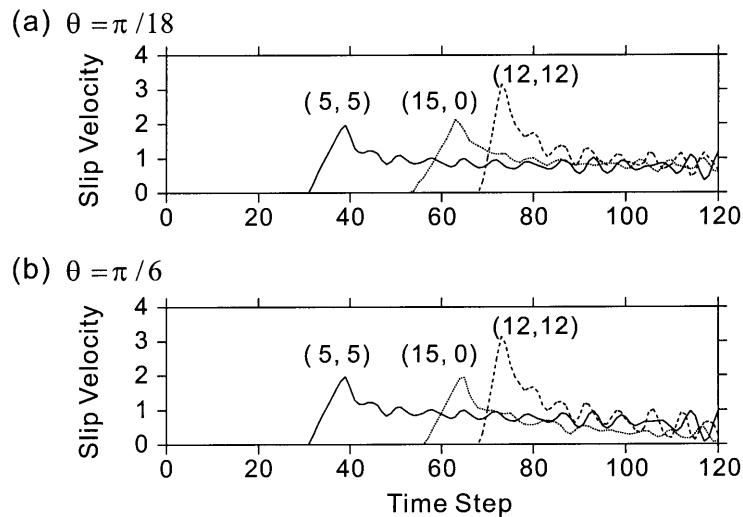
Figure 6
Slip velocities as a function of time step on various points on the curved fault. Cases (a) and (b) have the inclined angle $\theta = \pi/18$ and (b) $\pi/6$, which correspond to Figures 5(a) and (b), respectively.

Simulations of Kinked Fault

In order to examine the geometrical effect of the bend on dynamic rupture propagation, we show the difference of rupture propagation for various final angles of the secondary inclined fault θ, i.e., assuming, contrary to the previous case, that a uniform shear stress τ_{31}^{r0} applies upon the whole fault. In other words, the value of S is constant everywhere on the fault ($S = 1/3$). In Figure 7, we display snapshots of slip velocity on the fault at time step $t = 80$ (left four panels) and the total amount of slip at that time (right panel). The fault bends abruptly at $\xi_1 = 10.5$ with the angle (a) $\theta = \pi/18$ (b) $\pi/6$ (c) $\pi/3$ and (d) $\pi/2$, respectively. The numerical results show that rupture continues to propagate beyond the kinked portion with the same rupture velocity even though the fault bends perpendicularly. The effect of bending is more apparent on the slip distribution as shown in Figure 7. As the angle of bend becomes steeper, a lower slip region appears around the bending portion. This indicates that the bending portion acts as a kind of barrier in the rupture process. However, the results depend on the position of fault bending. When the bending is located near the initial crack, for example $\xi_1 = 5.5$, rupture does not propagate across the bend for the case of $\theta = \pi/2$, because of insufficient stress accumulation on the secondary bending fault.

TADA and YAMASHITA (1996) have pointed out the paradox that the opposite sign of normal stress appears on the fault for the analytical expression of the smooth bending fault and its numerical approximation with many small planar patches because of artificial kinks. However, our result shows that an artificial
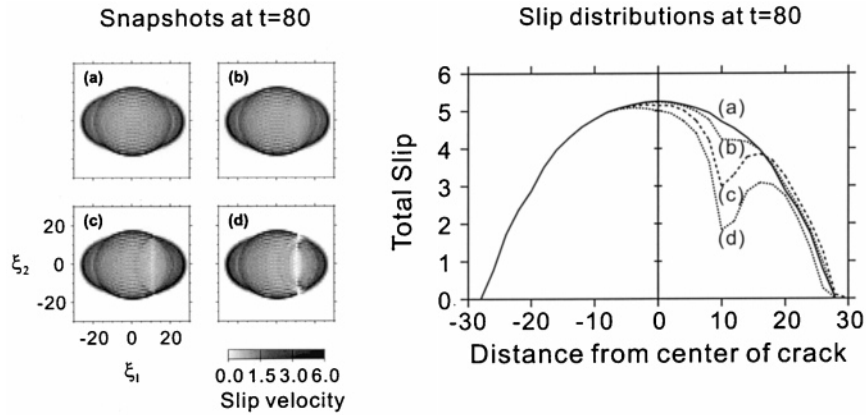
Figure 7

Difference in rupture propagation due to various final angles of the inclined fault. The fault bends abruptly at $\xi_1 = 10.5$ with the angle (a) $\theta = \pi/18$, (b) $\pi/6$, (c) $\pi/3$ and (d) $\pi/2$, respectively. The left figures show snapshots of slip velocity on the fault at time step $t = 80$, and the right one is the distribution of total amount of slip at the same time. Each rupture velocity of the crack front is only slightly different, although slip velocity around the bend is decelerated by the steep angle of the bend.

structure in which two planar grids connect with a finite angle produces no opposite polarity of stress field ahead of it, since rupture continues propagating without decreasing its rupture velocity for any angle of bend within $0 \leq \theta < \pi/2$. Here we must notice that the rupture growth is perfectly determined by the shear stress field on the fault in our simulations. Thus a series of planar small patches would be a proper approximation of a curved fault in the shear rupture model as long as we consider the fracture criterion which depends not on the normal traction but on the shear stress. We shall compare the models with different way of bending later.

Effect of Fault Angle

Now we return to the case of rupture propagation under the triaxial compression field. Figure 8 shows rupture fronts propagating in the direction of both the positive and negative ξ_1 directions at the cross section $\xi_2 = 0$ on various bending faults at the same residual stress level $\tau_r = 0$. Each geometry is shown at the top of the figure and the relation between the initial shear stress and the angle of the inclined fault is also shown in the case (c) of Figure 3. In the hypothetical situation where $\tau_{31}^{0}{}'$ is assumed to be constant everywhere as shown in Figure 7, we see no difference of rupture velocities for the angle of the secondary inclined fault, since energy balance between stored shear stress and consumed fracture energy around the crack tip is invariant, regardless of the bending angle. In the uniform triaxial compression field, however, we can find significant differences in rupture velocity
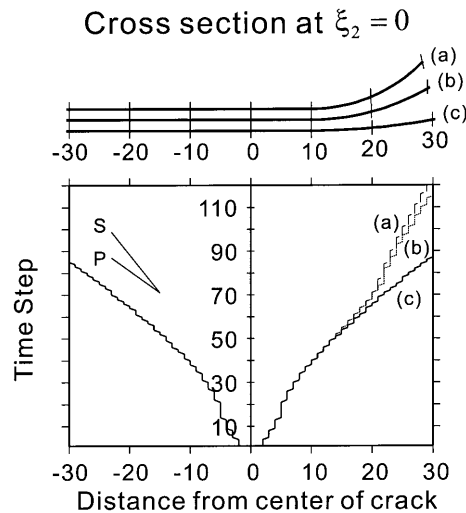
Cross section at $\xi_2 = 0$

Figure 8

Rupture propagation for various final angles of the inclined fault in the case of $\tau_r = 0$. At the top we show each geometry of the faults with the inclined angle (a) $\theta = \pi/4$, (b) $\pi/6$ and (c) $\pi/18$, respectively. Rupture velocity decreases with the initial stress level on the inclined fault.

between the three fault models, because the value of S depends on the final angle of the inclined fault θ. Rupture propagates with super-shear velocity for the case of $\theta = \pi/18$ which leads to $S = 0.42$, while rupture velocity remains below shear wave speed for above $\theta = \pi/6$ which corresponds to $S = 1.67$. Our result is consistent with DAS and AKI (1977) who reported that sub-shear velocity of rupture propagation requires S larger than 1.6 for 2-D in-plane problems.

Absolute Level of Residual Stress

Next we examine the effects of absolute level of residual stress on rupture propagation. We fix the final angle of the inclined fault θ to $\pi/6$ and change the residual stress level (a) $\tau_r = 5\Delta\tau_b$, (b) $\tau_r = 2\Delta\tau_b$ and (c) $\tau_r = 0$ as shown in Figure 9. For case (b) we have presented snapshots of rupture propagation in Figure 5(b). As absolute stress level increases, we observe that the rupture propagation beyond the fault bend becomes more difficult. In the case of $\tau_r \neq 0$, the rupture almost stops around the bending portion, while opposite side of the rupture front propagates further at a super-shear wave velocity. In fact, Figure 3 indicates that the initial shear stress becomes less than the residual stress level for an angle larger than about 15° in case (a), and 22° in case (b), respectively. These angles correspond to distances of about 15 and 18 from the center of the crack. For both cases, rupture proceeds slightly in the region where negative stress drop is brought about and then is arrested.
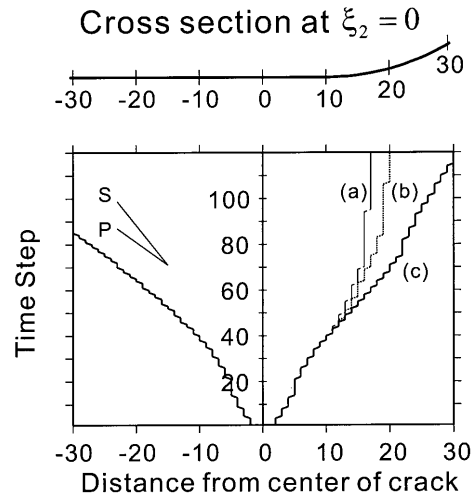
Figure 9

Rupture propagation for absolute stress level on the same bending fault, with final angle of the bending fault $\theta = \pi/6$ as shown at the top. Each case corresponds to (a) $\tau_r = 5\Delta\tau_b$, (b) $\tau_r = 2\Delta\tau_b$, and (c) $\tau_r = 0$, respectively. Rupture is nearly arrested around the bending for high residual stress level.

Kinked Fault and Smooth Curved Fault

Finally, we investigate the difference caused by the shape of bending. Figure 7 enables us to estimate that an artificial abrupt kink would produce no different result concerning rupture propagation, since the rupture velocity does not change significantly with the angle of the inclined fault. We consider a kinked fault which consists of two plane faults and a curved bending fault which we approximate with many small planar patches in order to understand its role. Figure 10 exhibits the difference in rupture propagation between two models for the case of $\tau_r = 5\Delta\tau_b$ (a, c) and $\tau_r = 0$ (b, d). Comparing (b) and (d), we can see that the terminal rupture velocities are almost the same in both cases, though the rupture propagates faster on the smooth curved fault (d), around the bending portion, than on the kinked fault (b). This phenomena can be interpreted in terms of the value of *S*. In the case of (d), the value of *S* increases gradually from 0.33 to 1.67. Conversely, it changes abruptly on the kinked fault (b). Similarly, the rupture propagates more smoothly for the curved fault (c) than for the kinked fault (a), which is considered to be caused by the pre-applied shear stress. For the inclined fault with angle $\pi/6$, the rupture necessarily produces a negative stress drop, as shown in Figure 3. Thus the rupture stops suddenly at the bending in case (a). We do not think that neither the effect of discretization nor approximation in modeling with many small planar patches produces any artificial result.
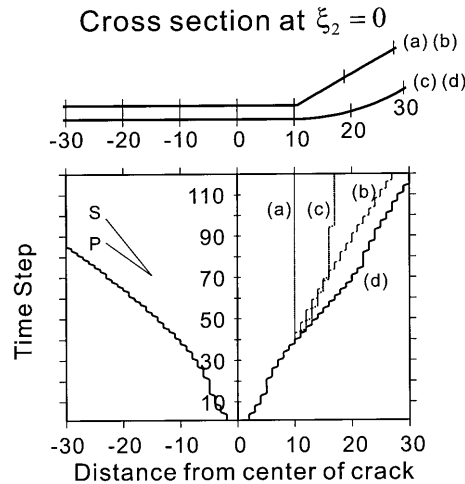
Cross section at $\xi_2 = 0$

Figure 10

Difference of rupture propagation between (a, b) kinked fault and (c, d) curved fault. Their geometries are drawn at the top of the figure and they have the same final angle of the bending fault $\theta = \pi/6$. We put $\tau_r = 5\Delta\tau_b$ for cases (a) and (c), and $\tau_r = 0$ for (b) and (d). The pre-loaded shear stress on the inclined fault produces the difference of the rupture propagation between that on the kinked and that on the smooth curved faults.

Discussion and Conclusion

In this paper we have constructed a new simulation scheme of spontaneous dynamic rupture propagation on non-planar faults in 3-D elastic medium. We removed all hyper-singularities in BIEs following the regularization method proposed by FUKUYAMA and MADARIAGA (1995, 1998), and also analytically evaluated all the BIEs for a basic box-like discrete source. This enables one to evaluate stress fields accurately and to simulate dynamic rupture propagation stably. This method is also applicable to rupture propagation on unknown paths in intact material, as KAME and YAMASHITA (1999a,b) simulated growths of a crack bending spontaneously in 2-D medium. Our BIE agrees with special case of the general formulation derived by TADA et al. (2000), and our scheme of simulation becomes the same as those proposed by FUKUYAMA and MADARIAGA (1995, 1998) for the case of a planar fault in 3-D.

As an example of numerical simulations, we considered a simple physical situation in which a bending fault is embedded in a 3-D elastic medium subjected to a uniform triaxial compression field. The simulation results demonstrate that rupture propagation is decelerated or arrested for some inclined angle of the bending fault and absolute value of the fault strength. We also observed that the effect of dynamic stress change caused by rupture propagation itself was not strong enough to stop the rupture propagation. The decrease of rupture velocity due to

bending also has been reported by BOUCHON and STREIFF (1997) in 2-D in-plane simulations. The velocity of rupture front depends mainly upon the pre-loaded initial stress on the fault with various directions of the inclined fault, that is, the parameter S. DAS and AKI (1977) and DAY (1982) examined the effect of S in 2-D anti- and in-plane cases and for a 3-D planar fault, respectively. Our results are consistent with theirs. For the special case of $S < 0$ in which negative stress drop occurs, we note that bending plays the role of a barrier strong enough to stop rupture propagation as naturally expected. In the field observation, the inversion result by WALD and HEATON (1995) shows that rupture velocity clearly changes with the strike direction of the fault, for example. From our results, we surmise that it is probably caused by the variation of pre-loaded shear stress on the faults.

We discussed the role of absolute value of shear stress level on rupture propagation. As it increases, it becomes more difficult for rupture to proceed on an inclined fault. The rupture propagation beyond the bend requires a low absolute level compared to breakdown strength drop $\Delta\tau_b$. From the inversion analysis by BOUCHON *et al.* (1998a) of the 1992 Landers earthquake, there exists a portion in which stress accumulation before rupture exceeds 20 MPa, although static stress does not change at all before and after earthquake on the fault with unfavorable strike. Assuming $\Delta\tau_b = 20$ MPa in the simulations we presented, for example, it would be difficult for the rupture to grow on a 30° inclined fault in the case of an absolute residual stress τ_r larger than 40 MPa (see Fig. 9). At the depth of 10 km, continuing pressure reaches 300 MPa, which leads to a frictional coefficient μ_f of 0.1–0.2, considerably smaller than that observed in the laboratory. This discussion, however, is constructed under the assumption that the fault system is embedded in such a homogeneous triaxial compression field as that in the simulations we demonstrated, and that the constitutive parameters are also homogeneous over the fault. The Landers earthquake might not be in such a simple state. AOCHI (1999) simulated the rupture propagation on the non-planar faults for that earthquake, considering a tectonic loading system, and discussed the physical background in detail.

In order to understand the physical process of earthquake generation, a forward modeling of dynamic rupture propagation on off-plane faults must be very efficient to reveal characteristics of the realistic field in which earthquakes occur. For this purpose we should model a more realistic condition using the scheme we have just constructed, and discussed in detail the effect of the complex geometrical structure of faults on earthquake generation.

provided us many valuable comments and suggestions for simplifying the formulations. We also express appreciation to Dr. Alain Cochard who reviewed and offered many valuable comments. For numerical study, we have used the computer system of Earthquake Information Center of Earthquake Research Institute, University of Tokyo, Japan.

Appendix A. Regularized Boundary Integral Equation

A Green's function in 3-D homogeneous, isotropic, infinite elastic medium (the Stokes tensor) is

$$G_{ij}(\vec{r}, t) = \frac{\beta^2}{4\pi\mu} \frac{3\gamma_i\gamma_j - \delta_{ij}}{r^3} \int_{r/\alpha}^{r/\beta} t'\delta(t - t')\, dt'$$

$$+ \frac{p^2}{4\pi\mu} \frac{\gamma_i\gamma_j}{r} \delta\left(t - \frac{r}{\alpha}\right) - \frac{1}{4\pi\mu} \frac{\gamma_i\gamma_j - \delta_{ij}}{r} \delta\left(t - \frac{r}{\beta}\right), \qquad \text{(A-1)}$$

where λ and μ are Lamé's constants, α and β are P- and S-wave velocities, respectively, $p = \beta/\alpha$, and $\delta(\cdot)$ is the delta function. The Laplace form of the integration appearing in equation (A-1)

$$\bar{I} = \int_0^\infty dt\, e^{-st} \frac{\beta^2}{r^2} \int_{r/\alpha}^{r/\beta} t'\delta(t - t')\, dt' = \frac{\beta^2}{r^2 s^2} \left\{ \left(1 + \frac{sr}{\alpha}\right) e^{-sr/\alpha} - \left(1 + \frac{sr}{\beta}\right) e^{-sr/\beta} \right\} \quad \text{(A-2)}$$

is useful for rewriting equation (2). For example, to obtain the off-plane expression ($x_3 \neq 0$) of the 3η component, we continue with equation (C8) in FUKUYAMA and MADARIAGA (1998), referred to as FM98 hereafter, without taking the limit $x_3 \to 0$. We rewrite equation (C9) and (C11) in FM98 for $x_3 \neq 0$, and then obtain the final expression instead of equation (C20) in FM98

$$\bar{\tau}_{3\eta}(\vec{x}, s) = -\frac{\mu}{4\pi} \int \frac{\gamma_\eta}{r^2} \Delta\bar{u}_{\zeta,\zeta}(\vec{\xi}, s) \left[12\bar{I} + 4p^2 e^{-sr/\alpha} - 5 e^{-sr/\beta} - \frac{sr}{\beta} e^{-sr/\beta} \right] d\Sigma$$

$$- \frac{\mu}{4\pi\beta^2} \int \frac{1}{r} s^2 \Delta\bar{u}_\eta(\vec{\xi}, s)\, e^{-sr/\beta}\, d\Sigma - \frac{\mu}{4\pi\beta} \int \frac{\gamma_\zeta}{r} s\Delta\bar{u}_{\eta,\zeta}(\vec{\xi}, s)\, e^{-sr/\beta}\, d\Sigma$$

$$- \frac{\mu}{4\pi} \int \frac{\gamma_\zeta}{r^2} \Delta\bar{u}_{\eta,\zeta}(\vec{\xi}, s)\, e^{-sr/\beta}\, d\Sigma + x_3^2 \frac{\mu}{\pi} \int \frac{\gamma_\eta}{r^4} \Delta\bar{u}_{\zeta,\zeta}(\vec{\xi}, s)$$

$$\times \left[15\bar{I} + 6p^2 e^{-sr/\alpha} - 6 e^{-sr/\beta} + \frac{sr}{\alpha} p^2 e^{-sr/\alpha} - \frac{sr}{\beta} e^{-sr/\beta} \right] d\Sigma, \qquad \text{(A-3)}$$

where $\bar{I}$ we defined here is (C10) in FM98 multiplied by (-1). When we take the limit $x_3 \to 0$, we can extract the instantaneous term from the third term in equation

(A-3) using (C17) in FM98, and then the above expression agrees with on-plane expression (C20) in FM98. Finally we derive the expression in time domain

$$
\begin{aligned}
\tau_{3\eta}(\vec{x}, t) = {} & \frac{\mu}{4\pi} \int \frac{\gamma_\eta}{r^2} \Bigg[-12 \frac{\beta^2}{r^2} \int_{r/\alpha}^{r/\beta} t' \Delta u_{\zeta,\zeta}(\vec{\xi}, \|t - t'\|)\, dt' - 4p^2 \Delta u_{\zeta,\zeta}\left(\vec{\xi}, \left\| t - \frac{r}{\alpha} \right\| \right) \\
& + 5\Delta u_{\zeta,\zeta}\left(\vec{\xi}, \left\| t - \frac{r}{\beta} \right\| \right) + \frac{r}{\beta}\, \Delta \dot{u}_{\zeta,\zeta}\left(\vec{\xi}, \left\| t - \frac{r}{\beta} \right\| \right) \Bigg] d\Sigma \\
& - \frac{\mu}{4\pi\beta^2} \int \frac{1}{r} \Delta \ddot{u}_\eta\left(\vec{\xi}, \left\| t - \frac{r}{\beta} \right\| \right) d\Sigma - \frac{\mu}{4\pi\beta} \int \frac{\gamma_\zeta}{r} \Delta \dot{u}_{\eta,\zeta}\left(\vec{\xi}, \left\| t - \frac{r}{\beta} \right\| \right) d\Sigma \\
& - \frac{\mu}{4\pi} \int \frac{\gamma_\zeta}{r^2} \Delta u_{\eta,\zeta}\left(\vec{\xi}, \left\| t - \frac{r}{\beta} \right\| \right) d\Sigma + \frac{\mu}{\pi} \int \frac{\gamma_3^2 \gamma_\eta}{r^2} \\
& \times \Bigg[15 \frac{\beta^2}{r^2} \int_{r/\alpha}^{r/\beta} t' \Delta u_{\zeta,\zeta}(\vec{\xi}, \|t - t'\|)\, dt' + 6p^2 \Delta u_{\zeta,\zeta}\left(\vec{\xi}, \left\| t - \frac{r}{\alpha} \right\| \right) \\
& - 6\Delta u_{\zeta,\zeta}\left(\vec{\xi}, \left\| t - \frac{r}{\beta} \right\| \right) + p^2 \frac{r}{\alpha}\, \Delta \dot{u}_{\zeta,\zeta}\left(\vec{\xi}, \left\| t - \frac{r}{\alpha} \right\| \right) \\
& - \frac{r}{\beta}\, \Delta \dot{u}_{\zeta,\zeta}\left(\vec{\xi}, \left\| t - \frac{r}{\beta} \right\| \right) \Bigg] d\Sigma,
\end{aligned} \tag{A-4}
$$

in which the slip functions $\Delta u_i(\|a\|)$ are only evaluated for positive values of a. In the limit $x_3 \to 0$ on equation (A-4), the instantaneous term ($\Delta \dot{u}$) is extracted from the 2nd term and the 5th off-plane term disappears.

Similarly we can derive the other components,

$$
\begin{aligned}
\tau_{33}(\vec{x}, t) = {} & \frac{\mu}{2\pi} \int \frac{\gamma_3}{r^2} \Bigg[-18 \frac{\beta^2}{r^2} \int_{r/\alpha}^{r/\beta} t' \Delta u_{\zeta,\zeta}(\vec{\xi}, \|t - t'\|)\, dt' + (1 - 8p^2)\Delta u_{\zeta,\zeta}\left(\vec{\xi}, \left\| t - \frac{r}{\alpha} \right\| \right) \\
& + 7\Delta u_{\zeta,\zeta}\left(\vec{\xi}, \left\| t - \frac{r}{\beta} \right\| \right) + (1 - 2p^2) \frac{r}{\alpha}\, \Delta \dot{u}_{\zeta,\zeta}\left(\vec{\xi}, \left\| t - \frac{r}{\alpha} \right\| \right) \\
& + \frac{r}{\beta}\, \Delta \dot{u}_{\zeta,\zeta}\left(\vec{\xi}, \left\| t - \frac{r}{\beta} \right\| \right) \Bigg] d\Sigma + \frac{\mu}{\pi} \int \frac{\gamma_3^3}{r^2} \\
& \times \Bigg[15 \frac{\beta^2}{r^2} \int_{r/\alpha}^{r/\beta} t' \Delta u_{\zeta,\zeta}(\vec{\xi}, \|t - t'\|)\, dt' + 6p^2 \Delta u_{\zeta,\zeta}\left(\vec{\xi}, \left\| t - \frac{r}{\alpha} \right\| \right) \\
& - 6\Delta u_{\zeta,\zeta}\left(\vec{\xi}, \left\| t - \frac{r}{\beta} \right\| \right) + p^2 \frac{r}{\alpha}\, \Delta \dot{u}_{\zeta,\zeta}\left(\vec{\xi}, \left\| t - \frac{r}{\alpha} \right\| \right) - \frac{r}{\beta}\, \Delta \dot{u}_{\zeta,\zeta}\left(\vec{\xi}, \left\| t - \frac{r}{\beta} \right\| \right), \Bigg] d\Sigma
\end{aligned} \tag{A-5}
$$

$$
\tau_{\eta\eta}(\vec{x}, t) = \frac{\mu}{2\pi} \int \frac{\gamma^3}{r^2} \Bigg[-6 \frac{\beta^2}{r^2} \int_{r/\alpha}^{r/\beta} t' \Delta u_{\zeta,\zeta}(\vec{\xi}, \|t - t'\|)\, dt' + (1 - 4p^2)\Delta u_{\zeta,\zeta}\left(\vec{\xi}, \left\| t - \frac{r}{\alpha} \right\| \right)
$$

$$+ 2\Delta u_{\zeta,\zeta}\left(\vec{\xi}, \left\|t - \frac{r}{\beta}\right\|\right) + (1 - 2p^2)\frac{r}{\alpha}\Delta\dot{u}_{\zeta,\zeta}\left(\vec{\xi}, \left\|t - \frac{r}{\alpha}\right\|\right)\right] d\Sigma$$

$$+ \frac{\mu}{\pi}\int \frac{\gamma_\eta^2\gamma_3}{r^2}\left[15\frac{\beta^2}{r^2}\int_{r/\alpha}^{r/\beta} t'\Delta u_{\zeta,\zeta}(\vec{\xi}, \|t - t'\|)\,dt' + 6p^2\Delta u_{\zeta,\zeta}\left(\vec{\xi}, \left\|t - \frac{r}{\alpha}\right\|\right)\right.$$

$$\left. - 6\Delta u_{\zeta,\zeta}\left(\vec{\xi}, \left\|t - \frac{r}{\beta}\right\|\right) + p^2\frac{r}{\alpha}\Delta\dot{u}_{\zeta,\zeta}\left(\vec{\xi}, \left\|t - \frac{r}{\alpha}\right\|\right) - \frac{r}{\beta}\Delta\dot{u}_{\zeta,\zeta}\left(\vec{\xi}, \left\|t - \frac{r}{\beta}\right\|\right)\right] d\Sigma$$

$$+ \frac{\mu}{2\pi}\int \frac{\gamma_3}{r^2}\left[\Delta u_{\eta,\eta}\left(\vec{\xi}, \left\|t - \frac{r}{\beta}\right\|\right) + \frac{r}{\beta}\Delta\dot{u}_{\eta,\eta}\left(\vec{\xi}, \left\|t - \frac{r}{\beta}\right\|\right)\right] d\Sigma, \qquad (A\text{-}6)$$

and

$$\tau_{12}(\vec{x}, t) = \frac{\mu}{\pi}\int \frac{\gamma_1\gamma_2\gamma_3}{r^2}\left[15\frac{\beta^2}{r^2}\int_{r/\alpha}^{r/\beta} t'\Delta u_{\zeta,\zeta}(\vec{\xi}, \|t - t'\|)\,dt' + 6p^2\Delta u_{\zeta,\zeta}\left(\vec{\xi}, \left\|t - \frac{r}{\alpha}\right\|\right)\right.$$

$$\left. - 6\Delta u_{\zeta,\zeta}\left(\vec{\xi}, \left\|t - \frac{r}{\beta}\right\|\right) + p^2\frac{r}{\alpha}\Delta\dot{u}_{\zeta,\zeta}\left(\vec{\xi}, \left\|t - \frac{r}{\alpha}\right\|\right)\right.$$

$$\left. - \frac{r}{\beta}\Delta\dot{u}_{\zeta,\zeta}\left(\vec{\xi}, \left\|t - \frac{r}{\beta}\right\|\right)\right] d\Sigma$$

$$+ \frac{\mu}{4\pi}\int \frac{\gamma_3}{r^2}\left[\Delta u_{\zeta,\bar{\zeta}}\left(\vec{\xi}, \left\|t - \frac{r}{\beta}\right\|\right) + \frac{r}{\beta}\Delta\dot{u}_{\zeta,\bar{\zeta}}\left(\vec{\xi}, \left\|t - \frac{r}{\beta}\right\|\right)\right] d\Sigma, \qquad (A\text{-}7)$$

where we define $\bar{\zeta} = 3 - \zeta$.

Appendix B. Discretized Kernel for a Semi-infinite Slip Velocity Field

We obtain the discretized kernels for the basic shear source given by equation (5). In this case, we can analytically evaluate all the integrals in equations (A-4)–(A-6) and (A-7), for discrete BIE without using any numerical calculation. We will introduce notations before summarizing discrete kernels,

$$\chi_\zeta'^2 = x_\zeta^2 + x_3^2, \quad X_\zeta(c) = \sqrt{c^2t^2 - \chi_\zeta'^2}, \quad \text{and} \quad \chi^2 = x_1^2 + x_2^2 + x_3^2 \qquad (B\text{-}1)$$

and

$$I_{i/\zeta} = \frac{x_i}{\chi_\zeta'^2}, \quad J_{ijk/\zeta} = \frac{x_i x_j x_k}{\chi_\zeta'^2}, \quad K_\zeta(c) = \frac{ct}{\chi_\zeta'}, \quad L_\zeta(c) = \frac{ctx_\zeta}{\chi}, \quad \text{and} \quad M(c) = \frac{ct}{\chi} \qquad (B\text{-}2)$$

and define three cases which depend on the observation point $\vec{x}$ and time t

$$\begin{cases} (I-c)_{\bar{\zeta}} & x_{\bar{\zeta}} < -X_{\zeta}(c) \quad \text{for} \quad X_{\zeta}(c)^2 > 0, \quad \text{or} \quad X_{\zeta}(c)^2 \leq 0 \\ (II-c) & \chi^2 < c^2 t^2 \\ (III-c)_{\bar{\zeta}} & x_{\bar{\zeta}} > X_{\zeta}(c) \quad \text{for} \quad X_{\zeta}(c)^2 > 0 \end{cases} \tag{B-3}$$

With the above notations and definitions, we create the final expressions of the discretized kernels

$$\tau_{31}(\vec{x}, t) = \frac{\mu}{4\pi\beta} \times [-V_1 E_{II}(\beta)$$

$$+ V_1(-Q_{11}(\beta) + Q_{11}(\alpha) + \mathcal{B}'_{11}(\beta) + R_{3311}(\beta) - R_{3311}(\alpha))$$

$$+ V_2(-Q_{12}(\beta) + Q_{12}(\alpha) + \mathcal{B}'_{12}(\beta) + R_{3312}(\beta) - R_{3312}(\alpha))], \tag{B-4}$$

$$\tau_{33}(\vec{x}, t) = \frac{\mu}{4\pi\beta} \times [V_1(-3(Q_{31}(\beta) - Q_{31}(\alpha)) + 2(\mathcal{B}'_{31}(\beta) - p(2p^2 - 1)\mathcal{B}'_{31}(\alpha))$$

$$+ R_{3331}(\beta) - R_{3331}(\alpha)) + V_2(-3(Q_{32}(\beta) - Q_{32}(\alpha))$$

$$+ 2(\mathcal{B}'_{32}(\beta) - p(2p^2 - 1)\mathcal{B}'_{32}(\alpha)) + R_{3332}(\beta) - R_{3332}(\alpha))], \tag{B-5}$$

$$\tau_{11}(\vec{x}, t) = \frac{\mu}{4\pi\beta} \times [V_1(-Q_{31}(\beta) + Q_{31}(\alpha) + 2(\mathcal{B}'_{31}(\beta) + p(1 - 2p^2)\mathcal{B}'_{31}(\alpha)) + R_{3111}(\beta)$$

$$- R_{3111}(\alpha)) + V_2(-Q_{32}(\beta) + Q_{32}(\alpha) + 2p(1 - 2p^2)\mathcal{B}'_{32}(\alpha)$$

$$+ R_{3112}(\beta) - R_{3112}(\alpha))], \tag{B-6}$$

$$\tau_{12}(\vec{x}, t) = \frac{\mu}{4\pi\beta} \times [V_1(-Q_{32}(\beta) + Q_{32}(\alpha) + \mathcal{B}'_{32}(\beta) + R_{3112}(\beta) - R_{3112}(\alpha))$$

$$+ V_2(-Q_{31}(\beta) + Q_{31}(\alpha) + \mathcal{B}'_{31}(\beta) + R_{3221}(\beta) - R_{3221}(\alpha))], \tag{B-7}$$

where we use the following 4 terms for the basic Heaviside function:

$$\mathcal{B}_{i\zeta}(c) \overset{i \neq \bar{\zeta}}{\to} \begin{cases} 0 & \text{for} \ (I-c)_{\bar{\zeta}} \\ I_{i/\zeta}(X_{\zeta}(c) + L_{\bar{\zeta}}(c)) & \text{for} \ (II-c) \\ 2I_{i/\zeta}X_{\zeta}(c) & \text{for} \ (III-c)_{\bar{\zeta}} \end{cases} \tag{B-8}$$

$$\overset{i = \bar{\zeta}}{\to} \begin{cases} 1 - M(c) & \text{for} \ (II-c) \\ 0 & \text{otherwise} \end{cases} \tag{B-9}$$

$$Q_{i\zeta}(c) \overset{i \neq \bar\zeta}{\to}$$

$$\begin{cases} 0 & \text{for } (\text{I}-c)_{\bar\zeta} \\ 2\dfrac{\beta^3}{c^3} I_{i/\zeta}\left[\dfrac{2}{3} X_\zeta(c)(1-K_\zeta(c)^2) + L_{\bar\zeta}(c)\left(1-\dfrac{1}{3}(M(c)^2+2K_\zeta(c)^2)\right)\right] & \text{for } (\text{II}-c) \\ \dfrac{8}{3}\dfrac{\beta^3}{c^3} I_{i/\zeta} X_\zeta(c)(1-K_\zeta(c)^2) & \text{for } (\text{III}-c)_{\bar\zeta} \end{cases}$$

$$(\text{B-10})$$

$$\overset{i=\bar\zeta}{\to} \begin{cases} 2\dfrac{\beta^3}{c^3}\left(\dfrac{2}{3}-M(c)\left(1-\dfrac{1}{3}M(c)^2\right)\right) & \text{for } (\text{II}-c) \\ 0 & \text{otherwise} \end{cases}$$

$$(\text{B-11})$$

$$R_{3ij\zeta}(c) \overset{i,j \neq \bar\zeta}{\to}$$

$$\begin{cases} 0 & \text{for } (\text{I}-c)_{\bar\zeta} \\ 2\dfrac{\beta^3}{c^3} J_{3ij/\zeta}\left[\dfrac{2}{3}\dfrac{X_\zeta(c)}{\chi_\zeta'^2}(1-4K_\zeta(c)^2) + \dfrac{L_{\bar\zeta}(c)}{c^2 t^2}\left\{(M(c)^2+2K_\zeta(c)^2)\left(1-\dfrac{4}{3}K_\zeta(c)^2\right)-M(c)^4\right\}\right] & \text{for } (\text{II}-c) \\ \dfrac{8}{3}\dfrac{\beta^3}{c^3} J_{3ij/\zeta}\dfrac{X_\zeta(c)}{\chi_\zeta'^2}(1-4K_\zeta(c)^2) & \text{for } (\text{III}-c)_{\bar\zeta} \end{cases}$$

$$(\text{B-12})$$

$$\overset{i=3,j=\bar\zeta}{\to} \begin{cases} -2\dfrac{\beta^3}{c^3}\dfrac{x_3^2}{\chi^2}M(c)(1-M(c)^2) & \text{for } (\text{II}-c) \\ 0 & \text{otherwise} \end{cases}$$

$$(\text{B-13})$$

$$\overset{i,j=\bar\zeta}{\to} \begin{cases} 0 & \text{for } (\text{I}-c)_{\bar\zeta} \\ 2\dfrac{\beta^3}{c^3} I_{3/\zeta}\left[\dfrac{2}{3}X_\zeta(c)(1-K_\zeta(c)^2) + \dfrac{x_\zeta^2}{\chi^2}L_{\bar\zeta}(c)\left(1-\dfrac{2}{3}K_\zeta(c)^2 - M(c)^2\right)\right] & \text{for } (\text{II}-c) \\ \dfrac{8}{3}\dfrac{\beta^3}{c^3} I_{3/\zeta} X_\zeta(c)(1-K_\zeta(c)^2) & \text{for } (\text{III}-c)_{\bar\zeta} \end{cases} \quad ,$$

$$(\text{B-14})$$

$$E_{II}(\beta) = 2\pi H(x_1)H(x_2)H(\beta t - |x_3|)$$

$$+ \sum_{\zeta=1}^{2} \begin{cases} 0 & \text{for} \quad (I - \beta)_{\bar{\zeta}} \\ I_{\zeta/\zeta}(X_\zeta(\beta) + L_{\bar{\zeta}}(\beta)) - \arctan\dfrac{X_\zeta(\beta)}{x_\zeta} - \arctan\dfrac{x_{\bar{\zeta}}}{x_\zeta} & \text{for} \quad (II - \beta) \\ 2\left(I_{\zeta/\zeta}X_\zeta(\beta) - \arctan\dfrac{X_\zeta(\beta)}{x_\zeta}\right) & \text{for} \quad (III - \beta)_{\bar{\zeta}} \end{cases} . \qquad \text{(B-15)}$$

Here $E_{II}(\beta)$ includes the instantaneous term.

All the discrete kernels derived in this appendix are the functions of the distance from the origin to an observation point. Substituting $(x_1 - \xi_1^l + \Delta s/2,\ x_2 - \xi_2^m + \Delta s/2;\ t - \tau + e_t\Delta t)$ for $(x_1, x_2; t)$ etc. we finally obtain the discrete kernels $P_{pq/\zeta}(\vec{r})$ for a piecewise source $\Delta\dot{u}_\zeta = S(\xi_1, \xi_2, \tau; \xi_1^l, \xi_2^m, \tau^n)$ that appears in equation (6).

REFERENCES

AKI, K., and RICHARDS, P. G., *Quantitative Seismology: Theory and Methods* (Freeman and Co., San Francisco 1980).

AOCHI, H. (1999), *Theoretical Studies on Dynamic Rupture Propagation along a 3-D Non-planar Fault System*, D.Sc. Thesis, University of Tokyo, Japan.

AYDIN, A., and DU, Y. (1995), *Surface Rupture at a Fault Bend: The 28 June 1992 Landers, California, Earthquake*, Bull. Seismol. Soc. Am. *85*, 111–128.

BOUCHON, M., CAMPILLO, M., and COTTON, F. (1998a), *Stress Field Associated with the Rupture of the 1992 Landers, California, Earthquake and its Implications Concerning the Fault Strength at the Onset of the Earthquake*, J. Geophys. Res. *103*, 21,091–21,097.

BOUCHON, M., SEKIGUCHI, H., IRIKURA, K., and IWATA, T. (1998b), *Some Characteristics of the Stress Field of the 1995 Hyogo-ken Nanbu (Kobe) Earthquake*, J. Geophys. Res. *103*, 24,271–24,282.

BOUCHON, M., and STREIFF, D. (1997), *Propagation of a Shear Crack on a Nonplanar Fault: A Method of Calculation*, Bull. Seismol. Soc. Am. *87*, 61–66.

COCHARD, A., and MADARIAGA, R. (1994), *Dynamic Faulting under Rate-dependent Friction*, Pure appl. geophys. *142*, 419–445.

DAS, S., and AKI, K. (1977), *A Numerical Study of Two-dimensional Spontaneous Rupture Propagation*, Geophys. J. R. astr. Soc. *50*, 643–668.

DAY, S. M. (1982), *Three-dimensional Simulation of Spontaneous Rupture: The Effect of Nonuniform Prestress*, Bull. Seismol. Soc. Am. *72*, 1881–1902.

ELLSWORTH, W. L., and BEROZA, G. C. (1995), *Seismic Evidence for an Earthquake Nucleation Phase*, Science *268*, 851–855.

FUKUYAMA, E., and MADARIAGA, R. (1995), *Integral Equation Method for Plane Crack with Arbitrary Shape in 3-D Elastic Medium*, Bull. Seismol. Soc. Am. *85*, 614–628.

FUKUYAMA, E., and MADARIAGA, R. (1998), *Rupture Dynamics of a Planar Fault in a 3-D Elastic Medium: Rate- and Slip-weakening Friction*, Bull. Seismol. Soc. Am. *88*, 1–17.

FUKUYAMA, E., and MADARIAGA, R. (2000), *Dynamic Rupture Propagation and Interaction of a Rupture Front on a Planar Fault*, Pure appl. geophys. *157*, 1959–1979.

HARRIS, R. A., and DAY, S. M. (1993), *Dynamics of Fault Interaction: Parallel Strike-slip Faults*, J. Geophys. Res. *98*, 4461–4472.

HARRIS, R. A., and DAY, S. M. (1999), *Dynamic 3-D Simulations of Earthquakes on en echelon Faults*, Geophys. Res. Lett. *26*, 2089–2092.

IDA, Y. (1972), *Cohesive Force across the Tip of a Longitudinal-shear Crack and Griffith's Specific Surface Energy*, J. Geophys. Res. *77*, 3796–3805.

IDE, S., and TAKEO, M. (1997), *Determination of Constitutive Relations of Fault Slip Based on Seismic Wave Analysis*, J. Geophys. Res. *102*, 27,379–27,391.

IRIKURA, K., IWATA, T., SEKIGUCHI, H., PITARKA, A., and KAMAE, K. (1996), *Lesson from the 1995 Hyogoken Nanbu Earthquake: Why Were such Destructive Motions Generated to Buildings?* J. Nat. Disaster Sci. *17*, 99–127.

KAME, N., and YAMASHITA, T. (1997), *Dynamic Nucleation Process of Shallow Earthquake Faulting in a Fault Zone*, Geophys. J. Int. *128*, 204–216.

KAME, N., and YAMASHITA, T. (1999a), *A New Light on Arresting Mechanism of Dynamic Earthquake Faulting*, Geophys. Res. Lett. *26*, 1997–2000.

KAME, N., and YAMASHITA, T. (1999b), *Simulation of the Spontaneous Growth of a Dynamic Crack without Constraints on the Crack Tip Path*, Geophys. J. Int. *139*, 345–358.

KASE, Y., and KUGE, K. (1998), *Numerical Simulation of Spontaneous Rupture Processes on two Non-coplanar Faults: The Effect of Geometry on Fault Interaction*, Geophys. J. Int. *135*, 911–922.

KOLLER, M. G., BONNET, M., and MADARIAGA, R. (1992), *Modeling of Dynamical Crack Propagation Using Time-domain Boundary Integral Equations*, Wave Motion. *16*, 339–366.

LAPUSTA, N., RICE, J. R., BEN-ZION, Y., and ZHENG, G.-T. (2000), *Elastodynamic Analysis for Slow Tectonic Loading with Spontaneous Rupture Episodes on Faults with Rate- and State-dependent Friction*, J. Geophys. Res., submitted.

MAGISTRALE, H., and DAY, S. M. (1999), *3-D Simulations of Multi-segment Thrust Fault Rupture*, Geophys. Res. Lett. *26*, 2093–2096.

MATSU'URA, M., KATAOKA, H., and SHIBAZAKI, B. (1992), *Slip-dependent Friction Law and Nucleation Processes in Earthquake Rupture*, Tectonophysics *211*, 135–148.

OKUBO, P. G., and DIETERICH, J. H. (1984), *Effects of Physical Fault Properties on Frictional Instabilities Produced on Simulated Fault*, J. Geophys. Res. *89*, 5817–5827.

OHNAKA, M. (1996), *Nonuniformity of the Constitutive Law Parameters for Shear Rupture and Quasistatic Nucleation to Dynamic Rupture: A Physical Model of Earthquake Generation Processes*, Proc. Natl. Acad. Sci. USA *93*, 3795–3802.

OHNAKA, M., KUWAHARA, Y., and YAMAMOTO, K. (1987), *Constitutive Relations between Dynamic Physical Parameters near a Tip of the Propagating Slip Zone during Stick-slip Shear Failure*, Tectonophysics *144*, 109–125.

PALMER, A. C., and RICE, J. R. (1973), *The Growth of Slip Surface in the Progressive Failure of Over-consolidated Clay*, Proc. Roy. Soc. Lond. A. *332*, 527–548.

SEELIG, TH., and GROSS, D. (1997), *Analysis of Dynamic Crack Propagation Using a Time-domain Boundary Integral Equation Method*, Int. J. Solids Struc. *34*, 2087–2103.

SEELIG, TH., and GROSS, D. (1999a), *On the Stress Wave Induced Curving of Fast Running Cracks—A Numerical Study by a Time-domain Boundary Element Method*, Acta Mechanica *132*, 47–61.

SEELIG, TH., and GROSS, D. (1999b), *On the Interaction and Branching of Fast Running Cracks—A Numerical Investigation*, J. Mech. Phys. Solids *47*, 935–952.

SEKIGUCHI, H., IRIKURA, K., IWATA, T., KAKEHI, Y., and HOSHIBA, M. (1996), *Minute Locating of Faulting beneath Kobe and the Waveform Inversion of the Source Process during the 1995 Hyogo-ken Nanbu, Japan, Earthquake Using Strong Ground Motion Records*, J. Phys. Earth. *44*, 473–487.

TADA, T., FUKUYAMA, E., and MADARIAGA, R. (2000), *Non-hypersingular Boundary Integral Equations for 3-D Non-planar Crack Dynamics*, Comput. Mech. *25*(6), 613–626.

TADA, T., and MADARIAGA, R. (2000), *Dynamic modeling of the flat 2-D Crack by a Semi-analytic BIEM Scheme*, Int. J. Num. Meth. Eng., submitted.

TADA, T., and YAMASHITA, T. (1996), *The Paradox of Smooth and Abrupt Bends in Two-dimensional In-plane Shear-crack Mechanics*, Geophys. J. Int. *127*, 795–800.

TADA, T., and YAMASHITA, T. (1997), *Non-hypersingular Boundary Integral Equations for Two-dimensional Non-planar Crack Analysis*, Geophys. J. Int. *130*, 269–282.

WALD, D. J., and HEATON, T. H. (1995), *Spatial and Temporal Distribution of Slip for the 1992 Landers, California, Earthquake*, Bull. Seismol. Soc. Am. *84*, 668–691.

YOSHIDA, S., KOKETSU, K., SHIBAZAKI, B., SAGIYA, T., KATO, T., and YOSHIDA, Y. (1996), *Joint Inversion of Near- and Far-field Waveforms and Geodetic Data for the Rupture Process of the 1995 Kobe Earthquake*, J. Phys. Earth. *44*, 437–454.